

Mapping the Dislocation Sub-Structure of Deformed Polycrystalline Ni by Scanning Microbeam Diffraction Topography

Brian Abbey^{1,2*}, Felix Hofmann¹, Jonathan Belnoue¹, Alexander Rack³, Remi Tucoulou³, Gareth Hughes⁴, Sophie Eve⁵, and Alexander M. Korsunsky¹

¹Department of Engineering Science, University of Oxford, Parks Road, Oxford, OX1 3PJ, UK.

²School of Physics, The University of Melbourne, Parkville, Victoria 3010, Australia.

³European Synchrotron Radiation Facility, F-38043 Grenoble, France.

⁴Department of Materials, University of Oxford, Parks Road, Oxford, OX1 3PJ, UK.

⁵ESCTM du CRISMAT – CNRT-Matériaux / ENSICAEN, 6 Boulevard Maréchal Juin, 14050 Caen Cedex 04, FRANCE

*Corresponding author: brian.abbey@eng.ox.ac.uk

When subjected to plastic deformation, individual grains within ductile FCC polycrystals fragment into relatively ‘soft’, low dislocation density cells separated by ‘hard’, dislocation-rich walls. Using a narrow bandwidth, sub-micrometer X-ray beam, we have mapped the deformation structure inside a single grain within a deformed Ni polycrystal. Dislocation multiplication and entanglement was found to vary depending on the physical dimensions of the grain. The method we use overcomes current limitations in classical X-ray topography allowing topographic images to be formed from small, highly deformed grains.

Imaging a highly perfect crystal via the two-dimensional detection of X-rays diffracted from its constituent lattice planes (diffraction topography) has been employed since the 1940's [1-3]. This technique has very different contrast mechanisms from those of conventional absorption imaging. Diffraction contrast, which can partly be accounted for by the dynamical theory of diffraction, allows visualisation of individual crystallographic line defects (dislocations) and local lattice strains [4]. Plastic deformation of metallic crystals is mediated by the formation and propagation of dislocations which self-organise into 'hard' dislocation-rich walls enclosing 'soft' regions of low dislocation density (cells) [5]. This dislocation patterning has profound consequences for material hardening and failure. However, because of lattice rotation between cells, ray-tracing from the diffraction image to the sample required for topography is not possible. This intrinsic problem of real and reciprocal space convolution has previously prevented X-ray topography from being used to image deformation structure within (poly) crystals [6].

Deconvolution of real and reciprocal space information may be achieved by reducing the size of the incident beam to the point where the cumulative amount of lattice curvature within the sampling volume is sufficiently small. The caveat to this is that the incident beam must contain a large enough spectral bandwidth to ensure all illuminated parts of the crystal remain in diffraction condition [7]. When using a broad bandwidth polychromatic ('white') incident beam however, quantitative interpretation of the data becomes significantly more challenging. By using the intense, narrow bandwidth ('pink') radiation from a single undulator peak we show here that all parts of the deformed crystal can be kept (partially) in diffraction, whilst the peak of the rocking curve can be determined via energy scanning. We hereafter

refer to the method of reconstructing a topographic image through the composition of multiple pink microbeam topographs as scanning microbeam diffraction topography (SMDT). In addition provided the incident beam is smaller than the length scale of the dislocation cells is used, the lattice rotation gradient and FWHM of the Bragg reflection provides a means of distinguishing between the individual cell walls and their ordered interiors [8].

Dislocations trapped in the crystal lattice via random interactions with one another are known as statistically stored dislocations (SSDs), whereas dislocations stored to accommodate inelastic lattice curvature are called geometrically necessary dislocations (GNDs) [9]. GND density varies approximately in accordance with the reciprocal of the local length scale of the deformation field (l) imposed by the sample structure; Fleck *et al.* [10] predicted that in polycrystals for $l < 20 \mu\text{m}$ the number density of GNDs should greatly exceed that of SSDs. The relative influence of crystallite size on plasticity behaviour is a topic of considerable interest due to its implications for the design and engineering of stronger and more resilient materials [11-13]. Although length scale dependence does not feature in classical continuum plasticity modelling [14] it is generally accepted that dislocation interactions must be responsible for size effects in plasticity. In spite of the great practical importance of polycrystalline metals, direct observation of the influence of size effects in dislocation structure formation within individual grains has not previously been reported.

In this letter the through-thickness deformation structure within the micrometer sized 'wedge' shaped grain loaded *in situ* has been mapped at very high spatial and angular resolution using SMDT. We note here that depth profiles of the dislocation tensor in

single crystals have previously been measured using white beam Laue diffraction and differential aperture X-ray microscopy (DAXM) [15]. X-ray topography inherently captures the fine structure of the individual Bragg spots and provides a significantly higher sensitivity to lattice misorientation. Electron backscatter diffraction (EBSD) allows the measurement of orientation in a shallow region (< 100 nm) near the grain surface. However, since the majority of the grain is buried, EBSD does not reveal the through-thickness dislocation structure of the grain, which is key to understanding its deformation behaviour. Figure 1 shows characterisation data of the 'micro-wedge'. The wedge makes a shallow 17.7° angle with the sample surface and reaches a maximum thickness of $7.6\text{ }\mu\text{m}$, after which it runs underneath grain A1 in the corner. At its thinnest point where the twin (A2) reaches the sample surface, the wedge grain thickness vanishes. The wedge geometry (Fig. 1d) allows us to distinguish between the influence of grain boundaries and the influence of the crystallite size. Due to the lattice orientation spread resulting from plastic deformation classical X-ray topography fails to produce an interpretable image of this sample.

Through-thickness orientation and lattice rotation values were confirmed using microbeam Laue diffraction measurements [16] made on beamline B16 at the Diamond Light Source (DLS) using a $5\times 5\text{ }\mu\text{m}$ parallel X-ray beam [17, 18]. The wedge grain was part of a $15\text{ }\mu\text{m}$ thick polycrystalline Ni foil sample which had been re-crystallised and annealed to minimise initial defect density. A schematic of the experimental SMDT geometry used on beamline ID22 at the European Synchrotron Radiation Facility (ESRF) in Grenoble, France is shown in Fig. 2. The X-ray beam was produced from the 2nd undulator harmonic; the peak photon energy could be varied from 15 to 18 keV with $\Delta E/E \sim 1\text{-}2\%$. Kirkpatrick-Baez (KB) mirrors were

used to produce a focused $0.6 \times 0.6 \mu\text{m}$ ($H \times V$) FWHM beam. A photodiode placed in the transmitted direct beam was used to record a scanning transmission X-ray microscopy (STXM) image. A thin scintillator screen was used to convert X-rays from the reflection under study to visible light. The luminescent image was magnified via a commercial microscope and projected onto a high resolution CCD camera (FReLoN) [19]. The CCD had 2048×2048 pixels of $14 \mu\text{m}$ giving an effective pixel size of $0.70 \mu\text{m}$ (20x objective) after magnification. The scintillator to sample distance was 50 mm giving an acceptance angle (measured across the diagonal) of 2.38° . The combined STXM and diffraction images (Fig. 2) make it possible to locate the grain precisely within the sample.

After initially stretching and relaxing the sample ($\sim 4\%$ plastic strain) the (220) reflection from the grain (exhibiting severe streaking – asterism [20]) was located and the undulator gap varied to find the peak energy. The KB mirrors were then installed and the focused beam raster scanned across the sample in $1 \mu\text{m}$ steps whilst the transmission and diffraction data were recorded (inset right, Fig. 2). A line scan capturing the rocking curve for the reflection at each point was made. With the knowledge of both the peak energy and Bragg angle (θ) we were able to determine elastic strain close to the grain boundary (see Fig. S1).

The sample was stretched a second time and held at $\sim 4\%$ strain. The topograph from the whole grain with $100 \times 100 \mu\text{m}$ beam (KB removed) at the peak energy (16.41 keV) is shown in Fig. 3a. The striking lack of any resemblance to the diffracting grain (or the incident box beam) is consistent with our earlier white beam topography studies. Before deformation the topograph resembles a point-for-point image of the

grain. After plastic deformation, lattice break-up and rotation within the grain mean the topograph cannot be corrected to provide a direct sample image. Fig. 3b shows a topograph collected from a region within the same grain having low dislocation density using a $0.6 \times 0.6 \mu\text{m}$ FWHM beam (KB installed). Most microbeam topographs collected from the interior of the grain show relatively minor streaking due to deformation since each small gauge volume contains only a small amount of cumulative lattice curvature. At the grain boundaries however, where the lattice curvature is greater, the microbeam topographs become significantly more streaked.

Figs. 3c and 3d show a compound SMDT topograph made up of 5041 (3c) and 2601 (3d) microbeam topographs, of grain B1 (see EBSD map in Fig. 1) before and after the final stretch. To form the compound image the centre-of-mass position of each microbeam topograph was located and added to a larger array, according to the piezo motor coordinates, removing the effect of large scale variations in θ across the grain. There are two areas of increased strain in the topographs; one is at the surface twin boundary labelled in Fig. 3c, the other at the corner of the grain where only the twin (grain A1) is visible in the EBSD map. After the final load increment, the deformation in these areas visibly increases.

Figs. 4a and 4b show the magnitude of the gradient and FWHM of the reflection in the θ plane respectively (corresponding data for χ is given in Fig. S2) for the grain before the final deformation step. Two dislocation depleted cells (L and M) surrounded by higher dislocation density walls based on the available FCC slip planes $\{111\}$, $\{1\bar{1}1\}$ and $\{1\bar{1}\bar{1}\}$ are identified. Analysis of the (220) reflection FWHM reveals the same dislocation structures (Fig 4b). The orientation for grain B1 matches

the observed slip directions. Since lattice rotation between dislocation cells and walls is expected to be much greater than the angular resolution of the experiment [21] however, features below the measurement resolution are detectable. Within the bulk part of the grain individual dislocation boundaries separating relatively dislocation free cells are visible, but moving toward the apex of the wedge these structures merge together.

From a naïve interpretation of the sample geometry we expect a greater cumulative number of dislocations to be present in the thicker part of the sample. In fact, the exact opposite is observed: the thinner the grain, the higher the dislocation density. This is indicated by the changes in both the lattice rotation and FWHM of the reflection (Fig 4d). There is no reason or evidence to suppose that the nature/orientation of the twin boundary is significantly different at the apex of the wedge than at any other point within the sample, hence we conclude that the differences in sub-grain deformation structure are size-dependent. For the rotation data, a peak is observed at around 1 μm , though in general the behaviour is close to linear. It is interesting to note that the FWHM, plotted as $\Delta K = \cos(\theta)(\Delta\theta)/\lambda$ (where λ is the photon wavelength) may be readily described by a power law of the form $\Delta K = k_0 + mt^{-N}$ (shown by the thin black line in Fig. 4g) where $m \sim 0.3$ and $N \sim 0.4$ and k_0 is an arbitrary constant. Both the Hall-Petch relationship and ordinary dislocation plasticity (ODP) mediated deformation [22] describing the influence of grain size (Hall-Petch) or sample dimensions (ODP) on the apparent strength of materials also follow a power-law behaviour. The difference in the trend of the FWHM and lattice rotation plots as a function of sample thickness is likely to be due to the fact that the FWHM data is dependent on the size of the coherent scattering

volume in addition to the strain which arises from the presence of dislocations [23, 24]. Fig 4 together with the 2D maps of the grain in Fig. 3 provide direct evidence for dislocations becoming trapped at the apex of the wedge. Further deformation of the sample produced only a moderate shift of both plots vertically and an increase in the dislocation density preferentially in the $\{1\bar{1}1\}$ plane.

In this letter we have demonstrated a method for recovering topographic images from highly plastically deformed, micrometer sized crystals which previously could not be imaged using conventional diffraction topography. Combined with the data from the position and FWHM analysis of the >16000 very high-angular resolution topographs collected during this study we have mapped the sub-grain dislocation structure within a single Ni grain. The data clearly indicate that a higher GND density occurs at reduced plastic length scales, interestingly this is the reverse of observations made in single crystals e.g. in nano-indentation experiments made on pillars [25]. A complete understanding of how a reduced grain size mediates dislocation activity has the potential to fundamentally influence our understanding of polycrystalline deformation. However this requires further advancement in the theoretical modelling of the relevant processes including dislocation entanglement and the redistribution of local stresses in order to match the experimental data presented here. The techniques we have described here will find immediate application in the study of several key phenomena including dislocation avalanches and strain bursts which have recently been reported [14]. In addition this work highlights the fact that X-rays can now be used to characterise the dislocation structure in a much larger range of samples than was previously possible, bridging the gap with, for example, electron microscopy.

The authors gratefully acknowledge Bernadette Domenges, of the LAMIPS lab in Caen (France) for FIB imaging and cross-sectioning work carried out on the earlier Ni foils. Financial support for this research from Rolls-Royce plc. and the Engineering and Physical Sciences Research Council (EPSRC) is also acknowledged.

References

1. Lang, A.R., *The projection topograph: a new method in X-ray diffraction microradiography*. Acta Crystallographica, 1958. **12**: p. 249-250.
2. Ramachandran, G.N., *X-ray Topographs of Diamond*. Proc. Indian Acad. Sci. Sect. A 19 280-292, 1944.
3. Wooster, N. and W.A. Wooster, *X-ray Topographs*. Nature, 1945. **155**: p. 786-787.
4. Tuomi, T., K. Naukkarinen, and P. Rabe, *Use of Synchrotron Radiation in X-ray Diffraction Topography*. Phys. Stat. Sol. (a), 1974. **25**(93): p. 93-106.
5. Mughrabi, H., *Dislocation wall and cell structures and long-range internal stresses in deformed metal crystals*. Acta Metallurgica, 1983. **31**(9): p. 1367-1379.
6. Polcarova, M. and J. Bradler, *Application of X-ray Diffraction Topography with a Monochromatic Divergent Beam to the Study of Distorted Crystals*. Journal of Applied Crystallography, 1987. **20**: p. 374-378.
7. Mellaert, L.J.v. and G.H. Schwuttke, *Feedback Control Scheme for Scanning X-ray Topography*. Journal of Applied Physics, 1972. **43**(2).
8. Levine, L.E., et al., *X-ray Microbeam measurements of individual dislocation cell elastic strains in deformed single-crystal copper*. Nature Materials, 2006. **5**.
9. Ashby, M.F., *The deformation of plastically non-homogeneous materials*. Philosophical magazine, 1969. **21**(170): p. 399-424.
10. Fleck, N.A., et al., *Strain gradient plasticity: theory and experiment*. Acta Metallurgica, 1993. **42**(2): p. 475-487.

11. Hall, E.O., *The Deformation and Ageing of Mild Steel: III Discussion of Results*. Proceedings of the Physical Society. Section B, 1951. **64**(747).
12. Petch, N.J., *Journal of Iron and Steel Instruments*, 1951. **174**.
13. Yip, S., *Nature*, 1998. **391**(532).
14. Csikor, F.F., et al., *Dislocation Avalanches, Strain Bursts, and the Problem of Plastic Forming at the Micrometer Scale*. *Science*, 2007. **318**.
15. Ice, G.E., et al., *At the limit of polychromatic microdiffraction*. *Materials Science and Engineering: A*, 2009. **524**(1-2): p. 3-9.
16. Barabash, R.I., et al., *White microbeam diffraction from distorted crystals*. *Applied Physics Letters*, 2001. **79**(6): p. 749-751.
17. Hofmann, F., et al., *Intragranular Lattice Misorientation Mapping by Synchrotron X-Ray Micro-Beams Laue VS Energy-Resolved Laue VS Monochromatic Reciprocal Space Analysis*. *International Journal of Modern Physics B*, 2010. **24**(1): p. 279-287.
18. Hofmann, F., et al., *Probing intra-granular deformation by micro-beam Laue diffraction*. *Mesomechanics*, 2009. **1**(1): p. 193-196.
19. Weitkamp, T., C. Raven, and A.A. Snigirev. *Imaging and microtomography facility at the ESRF beamline ID22*. in *Proceedings of SPIE*. 1999.
20. Honnycombe, R.W.K., *Inhomogeneity of Deformation in Metal Single Crystals*. Proceedings of the Physical Society. Section A, 1950. **63**: p. 672-673.
21. Jakobsen, B., et al., *Formation and Subdivision of Deformation Structures During Plastic Deformation*. *Science*, 2006. **312**: p. 889-892.
22. Stanford, N., U. Carlson, and M.R. Barnett, *Deformation twinning and the Hall-Petch relation in commercial purity Ti*. *Matall. Materials Transactions. A*, 2008. **39**: p. 934-944.

23. Ungar, T. and A. Borbely, *The effect of Dislocation Contrast on X-ray Line Broadening: A new Approach to Line Profile Analysis*. Applied Physics Letters, 1996. **69**(21).
24. Williamson, G.K. and W.H. Hall, *X-ray line broadening from fided aluminium and wolfram*. Acta Matallurgica, 1952. **1**(1): p. 22-31.
25. Bei, H., et al., *Compressive strengths of molybdenum alloy micro-pillars prepared using a new technique*. Scripta Materialia, 2007. **57**(5): p. 397-400.

Figures

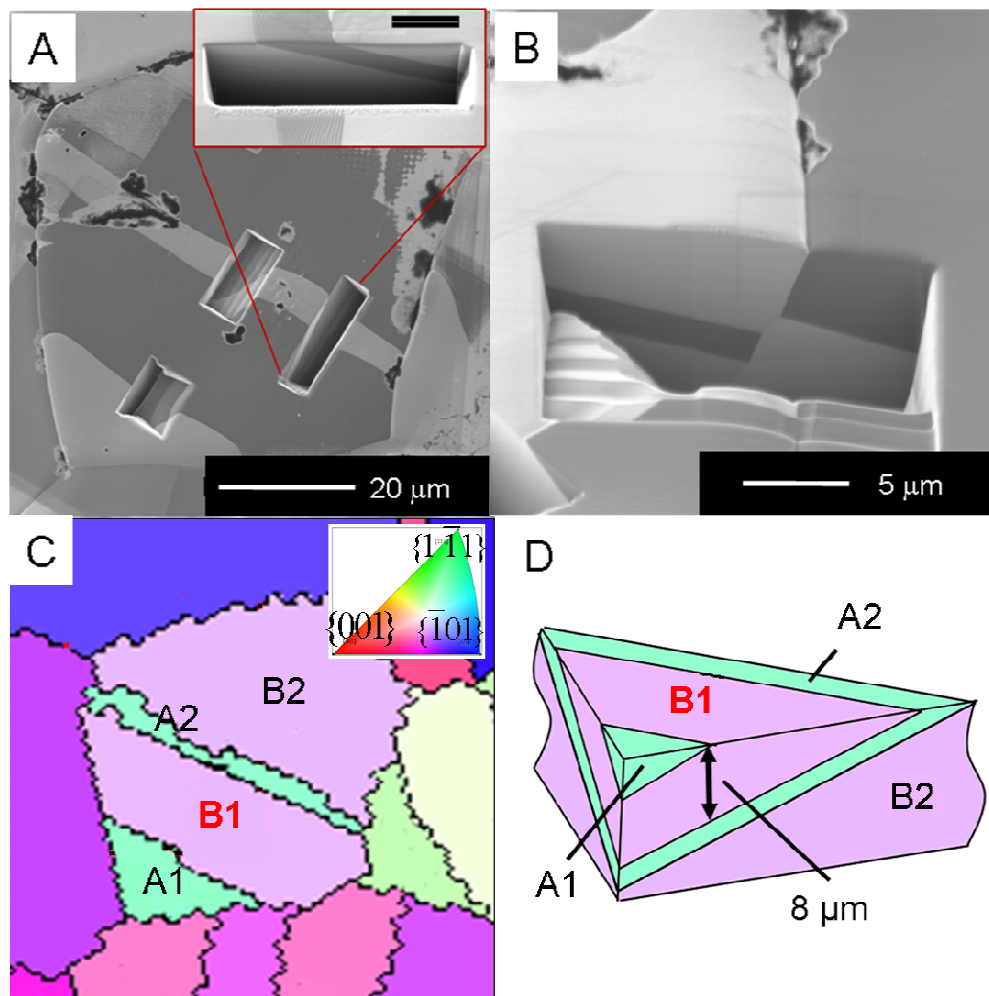


Fig. 1. Characterisation of the grain through focused ion beam (FIB) imaging with channelling contrast and cross sectioning and electron-backscatter diffraction (EBSD) (Colour online). (a) A post- X-ray measurement channelling contrast image of the whole wedge grain with several trenches visible, (inset) cross sectional cut showing angle of twin boundary (17.7 °) relative to sample surface. (b) Channelling contrast image of cross-section cut at grain boundary near to the point of maximum thickness of the micro-wedge grain (indicated by red 'B1' in c). (c) EBSD image of grain orientations within the scan region. (d) Schematic of 3D micro-wedge structure- the grain numbers correspond to (d).

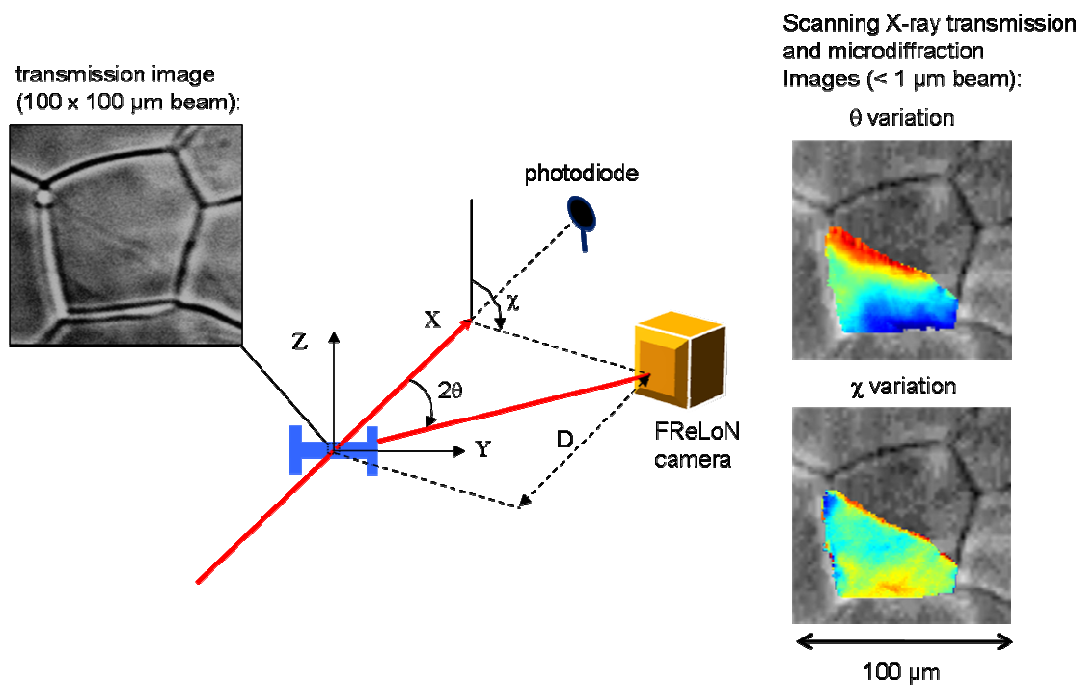


Fig. 2 **Schematic showing experimental geometry (Colour online).** (inset left) X-ray transmission image, (inset right) combined scanning transmission X-ray microscopy (STXM) and microdiffraction images. $D \sim 50$ mm, the effective pixel size of the detector was $0.70 \mu\text{m}$ providing a theoretical angular resolution of $14.3 \mu\text{rad/pixel}$.

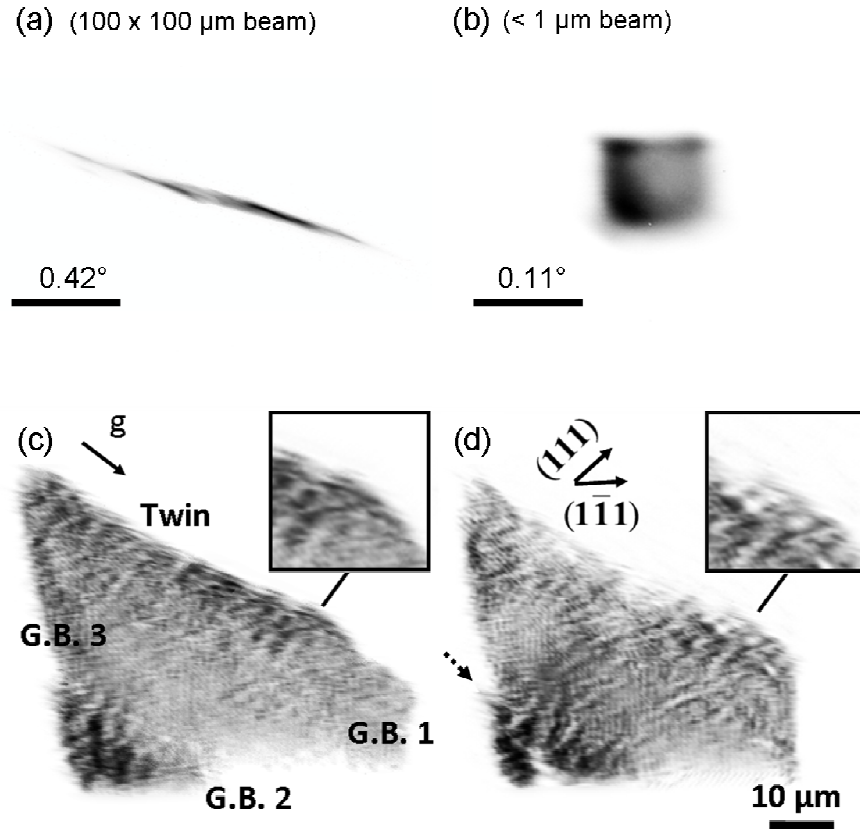


Fig. 3 Scanning microbeam diffraction data. (a) High resolution image of the (220) reflection from the whole grain (B1) taken with a 100 x 100 μm box beam at 16.41 keV. Image covers 1.68° horizontally and vertically (b) Image of a single microbeam topograph of the (220) reflection resembling the incident 0.61 x 0.61 μm sized beam incident upon a small sub-region within the grain. Image covers 0.42° horizontally and vertically (c) Composite of 5041 microbeam topographs showing the geometry of the partially buried plastically deformed grain studied in this letter. (d) Composite of 2601 microbeam topographs covering approximately 2/3 of the grain after further loading. The broken arrow indicates regions close to the grain boundary where severe streaking is observed. The two enlarged insets show the apex of the micro-wedge with significant lattice distortion.

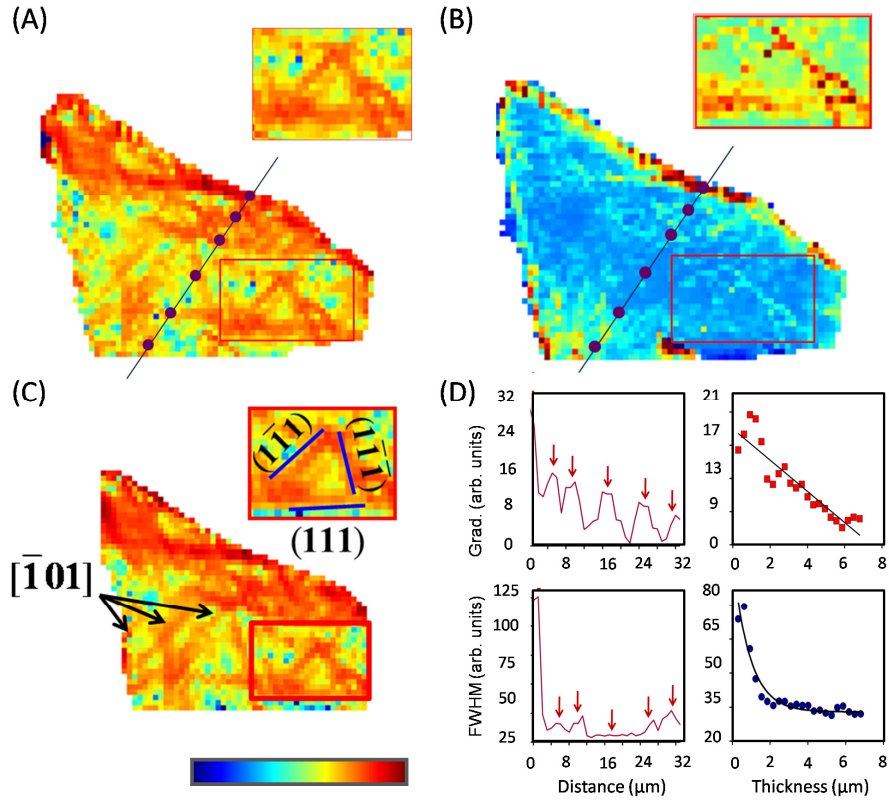


Fig 4. **Summary of microdiffraction analysis in the θ direction of grain (B1)** (Colour online). Note that all images are presented *without* any interpolation. (a) Magnitude of gradient and (b) FWHM of theta after first loading/unloading step, inset are enlargements of a dislocation cell. (c) Magnitude of gradient of theta after final loading to $\sim 4\%$ strain, plotted on same liner scale as (a). (d) Left - lineouts (indicated in a and b) showing the presence of dislocation boundaries in the rotation gradient and FWHM data, the red arrows mark identical positions on the two graphs. The width of the dislocation cell walls is between 1-2 μm and their separation is typically 4-10 μm . Right - the variation in the rotation gradient and FWHM in the theta direction as a function of sample thickness. The two plots represent an average of all the data in the grain grouped into 0.3 μm bins according to sample thickness. In both cases as the sample thickness (sample volume) decreases, the rotation gradient and FWHM increase.